Chip-integrated ultrafast graphene photodetector with high responsivity

Xuetao Gan[1†], Ren-Jye Shiue[2†], Yuanda Gao[3], Inanc Meric[1], Tony F. Heinz[1,4], Kenneth Shepard[1], James Hone[3], Solomon Assefa[5] and Dirk Englund[1,2]★

Graphene-based photodetectors have attracted strong interest for their exceptional physical properties, which include an ultra-fast response[1-3] across a broad spectrum[4], a strong electron–electron interaction[5] and photocarrier multiplication[6-8]. However, the weak optical absorption of graphene[2,3] limits its photoresponsivity. To address this, graphene has been integrated into nanocavities[9], microcavities[10] and plasmon resonators[11,12], but these approaches restrict photodetection to narrow bands. Hybrid graphene–quantum dot architectures can greatly improve responsivity[13], but at the cost of response speed. Here, we demonstrate a waveguide-integrated graphene photodetector that simultaneously exhibits high responsivity, high speed and broad spectral bandwidth. Using a metal-doped graphene junction coupled evanescently to the waveguide, the detector achieves a photoresponsivity exceeding $0.1\,\mathrm{A\,W^{-1}}$ together with a nearly uniform response between 1,450 and 1,590 nm. Under zero-bias operation, we demonstrate response rates exceeding 20 GHz and an instrumentation-limited 12 Gbit s^{-1} optical data link.

Graphene demonstrates ultrafast carrier dynamics for both electrons and holes, and it has been shown that a weak internal electric field allows high-speed and efficient photocarrier separation[2,3,14]. Moreover, graphene's two-dimensional nature appears to enable the generation of multiple electron–hole pairs for every high-energy photon excitation[6-8]. This carrier multiplication process is equivalent to inherent gain in graphene photodetection, which exists even without external bias, unlike traditional avalanche detection[15]. Despite these attractive features, the low optical absorption in graphene results in low photoresponsivity in vertical-incidence photodetector designs.

Recently it has been revealed that coupling graphene to a bus waveguide can enhance light absorption over a broadband spectrum[16,17]. Here, we show that, by integrating a graphene photodetector onto a silicon-on-insulator (SOI) bus waveguide, it is possible to greatly enhance graphene absorption and the corresponding photodetection efficiency without sacrificing the high speed and broad spectral bandwidth. In our device, presented in Fig. 1a, a silicon waveguide is backfilled with SiO$_2$ and then planarized to provide a smooth surface for the deposition of graphene. A thin SiO$_2$ layer (∼10 nm) deposited on the planarized chip electrically isolates the graphene layer from the underlying silicon structures. The optical waveguide mode couples to the graphene layer through the evanescent field, leading to optical absorption and the generation of photocarriers. Two metal electrodes located on opposite sides of the waveguide collect the photocurrent. One of these electrodes is positioned ∼100 nm from the edge of the waveguide to create a lateral metal-doped junction that overlaps with the waveguide mode. The junction is close enough to the waveguide to efficiently separate the photoexcited electron–hole pairs at zero bias, but the metal contact–waveguide separation of 100 nm is still far enough to ensure that the optical absorption is dominated by graphene to limit optical absorption.

Figure 1b presents an optical microscope image of one of the fabricated photodetector devices, and Fig. 1c displays a close-up scanning electron microscope (SEM) image of the device. This device contains a 53-µm-long graphene bilayer, which provides approximately twice the absorption of monolayer graphene. The graphene sheet was mechanically exfoliated and transferred onto the waveguide. The two electrodes were created by liftoff patterning with separations of 100 nm and 3.5 µm from the edges of the waveguide, respectively. The fabrication of this chip-integrated graphene photodetector (see Methods) requires only two lithography steps and no implantation, making it potentially simpler than the heterogeneous integration of other semiconductors[18,19].
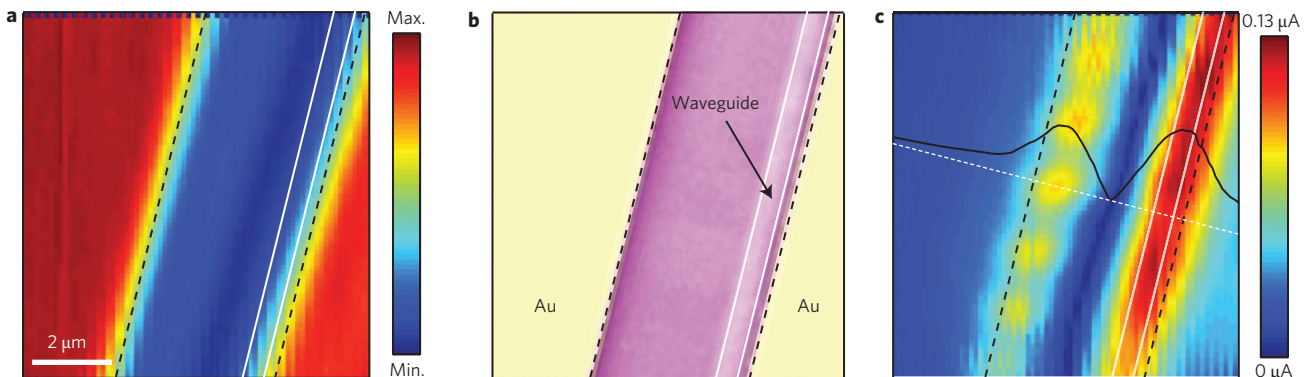
Spatially resolved photocurrent measurements were used to confirm the integrity of the metal-doped graphene junction. The sample was mounted under a confocal microscope on an x–y translation stage and illuminated from above with a 1,550 nm continuous-wave (c.w.) laser. A scanning reflectivity image of the device (Fig. 2a) shows the overall device structure, with the metal electrodes exhibiting higher reflectivity than the silicon and SiO$_2$ regions. By correlating the metal edges in the reflection image to those in the corresponding SEM image of the measured section (Fig. 2b), we obtained the location of the silicon waveguide (indicated by the solid white lines in Fig. 2a–c). Figure 2c maps the photocurrent obtained under zero bias voltage. The two narrow regions of high photocurrent along the metal/graphene boundaries indicate the expected built-in electric field between the metal-doped graphene and the bulk graphene region. The metal-doped junction not only exists at the metal/graphene interface, but also extends into the graphene channel between the two electrodes[20,21]. Because of the approximately micrometre-scale spot size of the excitation laser, we also observed photocurrent under the metal electrodes. The region of greatest photocurrent coincided with the waveguide and reached 13 nA, corresponding here to an excitation power of 50 µW measured after the objective lens. This responsivity of $2.6 \times 10^{-4}\,\mathrm{A\,W^{-1}}$ corresponds to the low photodetection efficiency of a graphene photodetector as expected for normal-incidence excitation[2,3].

By deconvolving the photocurrent profile plotted in Fig. 2c with the spot size of the excitation laser and numerically integrating it along the dashed white line, a relative potential profile across the graphene channel is obtained[20], as shown in the top part of Fig. 3a.

[1]Department of Electrical Engineering, Columbia University, New York, New York 10027, USA, [2]Department of Electrical Engineering and Computer Science, Massachusetts Institute of Technology, Cambridge, Massachusetts 02139, USA, [3]Department of Mechanical Engineering, Columbia University, New York, New York 10027, USA, [4]Department of Physics, Columbia University, New York, New York 10027, USA, [5]IBM T. J. Watson Research Center, Yorktown Heights, New York 10598, USA; [†]These authors contributed equally to this work. *e-mail: englund@mit.edu
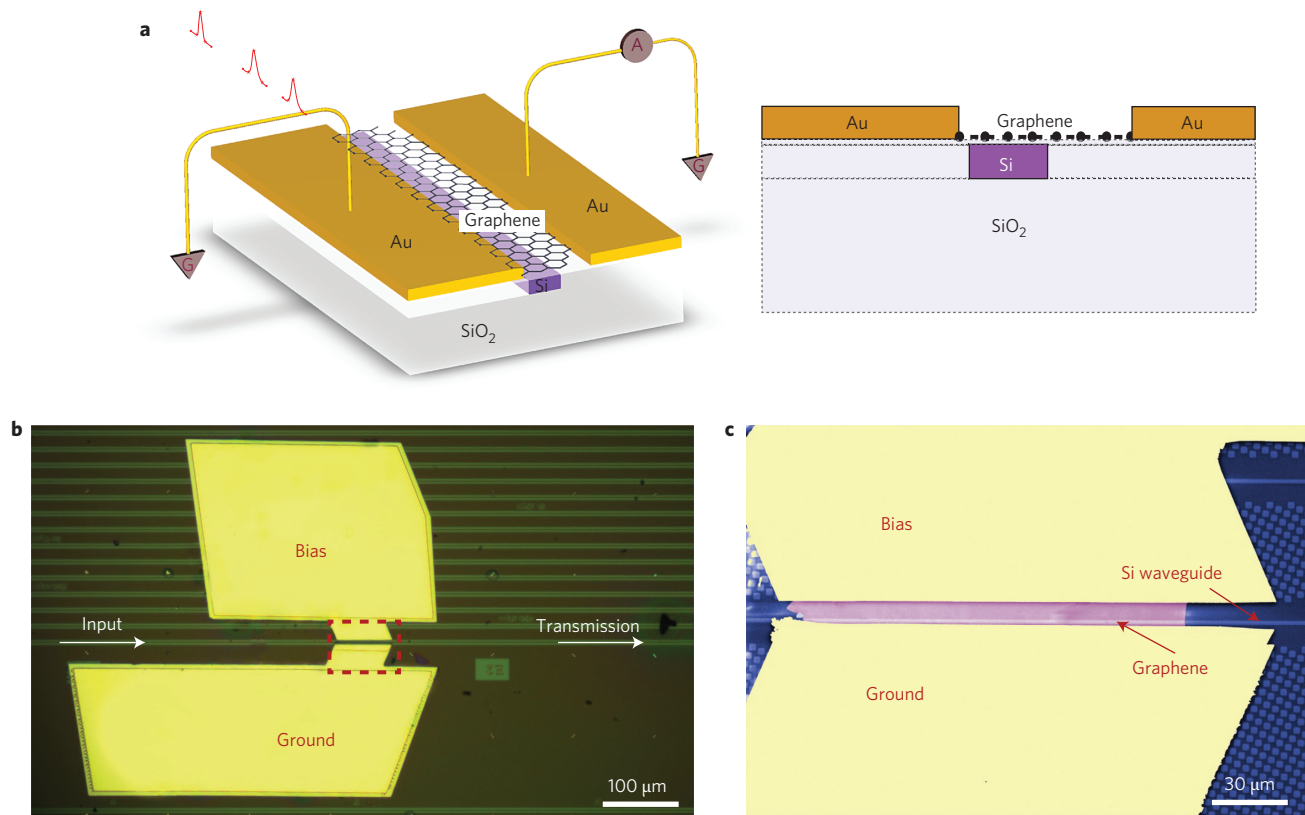
Figure 1 | A waveguide-integrated graphene photodetector. a, Schematic of the device. The silicon bus waveguide fabricated on an SOI wafer is planarized using SiO$_2$. A graphene layer is transferred onto the planarized waveguide with a spacing layer of ∼10-nm-thick SiO$_2$. Two metal electrodes contact the graphene and conduct the generated photocurrent. One of the electrodes is closer to the waveguide to create a potential difference in the graphene to couple with the evanescent optical field of the waveguide. **b**, Optical microscopy top view of the device with a bilayer of graphene covering the waveguide, which is evaporated with two titanium/gold (1/40 nm) paddles. **c**, SEM image showing the boxed region in **b** (false colour), displaying the planarized waveguide (blue), graphene (purple) and metal electrodes (yellow).

Figure 2 | Metal-doped junctions at the metal/graphene interfaces of the device determined by measuring a spatially resolved photocurrent on a confocal microscope set-up with top illumination. a, Scanning reflection image of the device, indicating the edges of the metal electrodes. **b**, SEM image of the measured section of the device. The waveguide is located by correlating the reflection image in **a** and the SEM image. **c**, Spatially resolved photocurrent (amplitude) image measured at zero bias voltage, representing two photocurrent strips around the metal/graphene interfaces. A photocurrent profile plotted along the dashed white line is superposed on the image. Scale bar applies to all panels. Dashed black and solid white lines show the edges of the metal electrodes and the waveguide, respectively. The scanning photocurrent image indicates narrow junctions at the metal/graphene interfaces, one of which overlaps with the waveguide.

The result shows that the graphene has potential gradients around the boundaries of the gold electrodes, yielding the corresponding internal electric field[21]. The graphene beneath the two metal contacts has the same p-type doping level, which is lower than the intrinsic doping of the graphene channel. Therefore, band bending with opposing gradients occurs at the two electrode junctions. The bottom panel of Fig. 3a presents the simulated transverse electric (TE) mode of the silicon waveguide, which is coupled to the bilayer graphene (dashed white line) and the two metal electrodes (orange rectangle). We also plot the field distribution along the graphene sheet (red curve), which corresponds to the photocarrier density. Here, the top and bottom images are aligned horizontally according to the position of the waveguide. It is thus evident that a strong potential gradient overlaps with the waveguide mode. In addition, the absence of an overlap

between the optical field and the potential difference created by the left electrode shown in Fig. 3a ensures the acceleration of electrons (or holes) only in one direction and the absence of cancellation in the net photocurrent[2,3]. Therefore, our optimized asymmetric metal electrode design provides a high internal quantum efficiency for collecting photocarriers.

In testing the performance of the waveguide-integrated graphene detector, light was coupled from lensed fibres into and out of the waveguide via SU8 edge couplers at opposite ends of the silicon waveguide. The polarization of the input was controlled to match the TE mode of the waveguide. From waveguide transmission measurements before and after the graphene transfer, we estimate a transmission loss of 4.8 dB caused by the 53-μm-long graphene bilayer, which is much greater than the 0.1 dB absorption in the normal-incidence configuration. The transmission loss indicates an absorption coefficient of 0.09 dB μm^{-1}. Estimating the absorption from the complex effective index of the simulated guided mode, we obtain a slightly lower absorption coefficient of 0.085 dB μm^{-1} for a graphene bilayer. We attribute the greater absorption coefficient obtained in the current device to the extra scattering and back-reflection caused by the graphene/waveguide interface. From the simulation, we also calculated the contribution of the 40-nm-thick metal contact to the total waveguide absorption,

which indicates an absorption coefficient of $\sim$0.009 dB μm^{-1}. Thus, we conclude that the graphene layer is responsible for $\sim$90% of the absorption of the waveguide.

To measure the photodetection efficiency of the device, we modulated a 1,550 nm c.w. input laser at a low frequency and detected the photocurrent through a preamplifier and a lock-in amplifier. Figure 3b plots the detected photocurrent (I_{photo}) as a function of incident power (P_{input}) obtained at zero bias voltage ($V_B = 0$). Here, P_{input} is the power reaching the waveguide-graphene detector, estimated by considering the input facet coupling loss and the silicon waveguide transmission loss. This measurement indicates an external responsivity (I_{photo}/P_{input}) of 15.7 mA W^{-1}, two orders of magnitude higher than that obtained for normal incidence. We attribute this dramatic responsivity improvement to the longer light–graphene interaction and the efficient separation of the photo-excited electron–hole pairs resulting from the strong local electric field across the metal-doped junction. Moreover, the curve plotted in Fig. 3b shows that the photocurrent approaches zero linearly under low-power optical excitation, which indicates vanishing dark current under zero-bias operation.

It was possible to further enhance the external responsivity by applying a bias voltage V_B across the photocarrier generation region. The results are shown in Fig. 3c, plotted here after
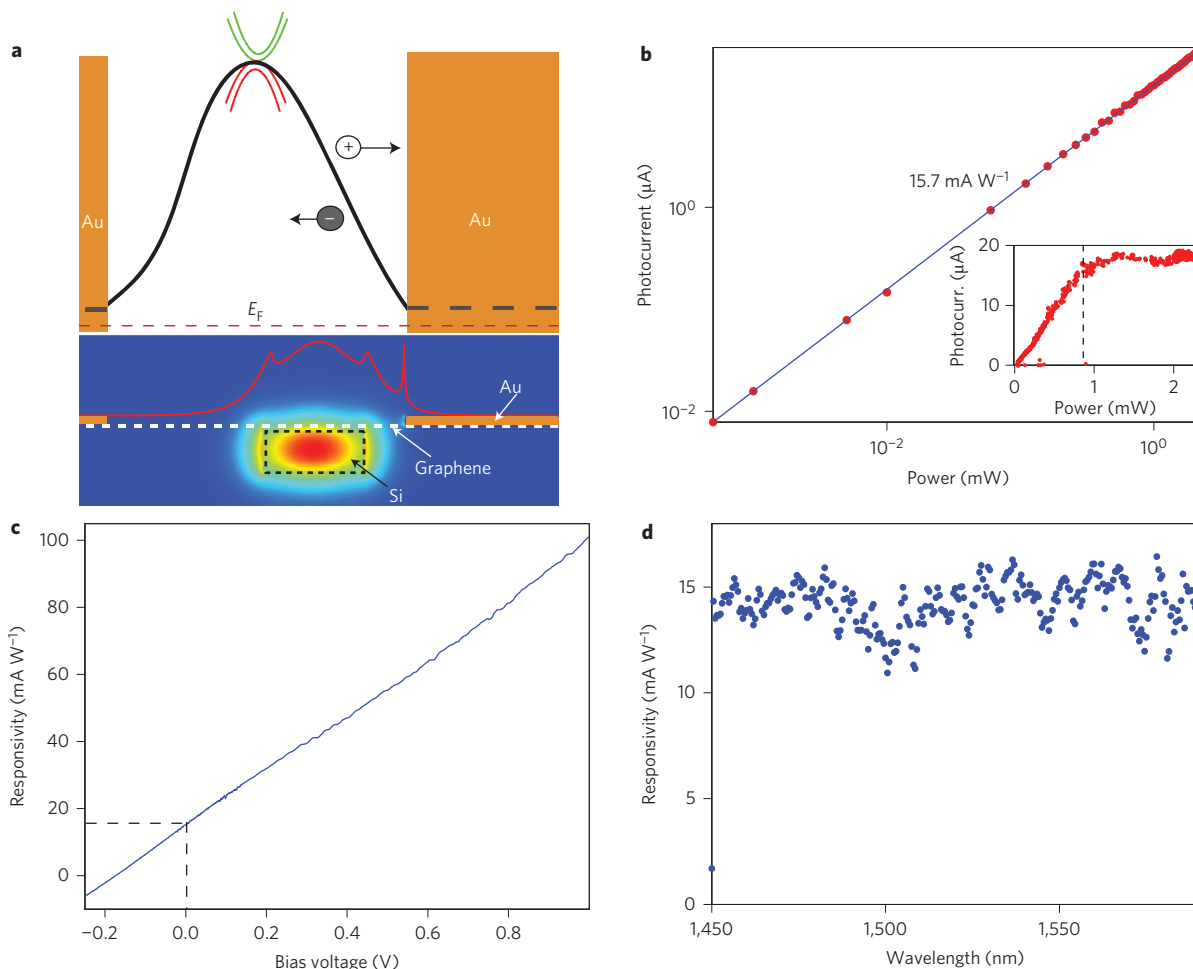
Figure 3 | Photoresponse of the waveguide-integrated graphene bilayer when excited through the waveguide. a, Top: potential profile (black solid line) across the graphene channel, showing band bending around the two metal electrodes. The red dashed line denotes the Fermi level. Bottom: simulated electric field of the TE waveguide mode. The field intensity at the graphene position is shown as a red line. The top and bottom images are aligned horizontally by referring to the relative position of the waveguide; the position of the right electrode is symbolic. **b**, Measured photocurrent with respect to the incident power of a c.w. laser at zero bias. Inset: photocurrent as a function of excited power from a pulsed OPO laser at a wavelength of 2,000 nm. **c**, Bias dependence of the photoresponsivity. **d**, Broadband uniform responsivity over a wavelength range from 1,450 nm to 1,590 nm at zero bias.

subtracting the dark current. When $V_B > 0$, the external bias induces an additional electric field along the direction of the built-in field and therefore enhances the separation of photocarriers, increasing the responsivity to a value as high as 0.108 A W^{-1} at $V_B = 1$ V. If $V_B < 0$, the photocurrent decreases due to compensation between the external and internal fields, and vanishes for $V_B = -175$ mV. The photocurrent changes sign when the bias is decreased further. Note that the responsivity is linear with respect to the bias voltage, without saturation even under a high bias, which indicates that the wide evanescent field of the waveguide excites a large charge carrier density in the graphene layer. Thus, an even higher photocurrent is expected under increased bias. To suppress the enhanced dark current for high bias voltages, future studies may induce a bandgap in the bilayer graphene by the application of a strong perpendicular electric field[22,23].

Owing to the spectrally flat absorption of graphene, a uniform photoresponse is expected across a wide range of wavelengths. Experimentally, we indeed observed a nearly flat photocurrent in spectrally resolved photodetection measurements under zero bias from 1,450 nm to 1,590 nm for a fixed optical input power, as shown in Fig. 3d. The flat response suggests the possibility of carrier multiplication, as recently reported in vertical-incidence experiments[8], although further studies are needed to confirm this effect in the waveguide configuration. The long absorption length of the graphene sheet may be expected to enable operation even at high power, because any saturation towards the front of the graphene would be compensated by additional absorption further along the waveguide. Indeed, experimentally we observed no saturation of photocurrent under c.w. laser excitation for launching powers up to 10 dBm into the detector. Photoresponse measurements were also performed using a pulsed optical parametric oscillator (OPO) source at a wavelength of 2,000 nm. The pulse duration was 250 fs. The inset to Fig. 3b shows the photocurrent as a function of the average incident power of the OPO pulsed source, indicating a saturation of the photocurrent for an incident power near 760 μW. We estimate that, under these conditions, the graphene layer experiences a peak intensity of 6.1 GW cm^{-2}, similar to the threshold of saturable absorption in graphene due to Pauli blocking[24].

Unlike the case in conventional semiconductors, both electrons and holes in graphene have very high mobility, and a moderate internal electric field allows ultrafast and efficient photocarrier separation. We examined the high-speed response of the device using a commercial lightwave component analyser (LCA) with an internal laser source and network analyser over a frequency range from 0.13 GHz to 20 GHz. A modulated optical signal at a wavelength of 1,550 nm with an average power of 1 mW emitted from the LCA was coupled into the device, and the electrical output was measured through a radiofrequency microwave probe. The frequency response of the device was analysed as the S_{21} parameter of the network analyser. Figure 4 displays the a.c. photoresponse of the device at zero bias, showing ~1 dB degradation of the signal at 20 GHz. Because the extremely high carrier mobility of graphene is estimated to result in an intrinsic photoresponse faster than 640 GHz (ref. 2), the limited dynamic response can be attributed to a large capacitance from the relatively large device area.

To gauge the viability of the waveguide-integrated graphene photodetector in realistic optical applications, we performed an optical data transmission at 12 Gbit s^{-1}. A pulsed pattern generator with a maximum 12 Gbit s^{-1} internal electrical bit stream modulated a 1,550 nm c.w. laser via an electrooptic modulator. About 10 dBm average optical power was launched into the waveguide graphene detector. The output electrical data stream from the graphene detector was amplified and sent to a digital communication analyser to obtain an eye diagram (see Methods for details). As shown in the inset of Fig. 4, a clear eye-opening diagram, at 12 Gbit s^{-1}, was obtained. Because of the frequency limitation of the pulse pattern
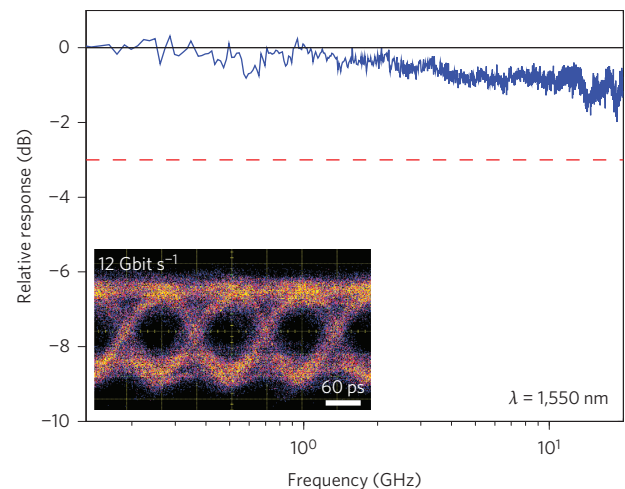
Figure 4 | Dynamic optoelectrical response of the device. The relative a.c. photoresponse as a function of light intensity modulation frequency shows ~1 dB degradation of the signal at a frequency of 20 GHz. Inset: 12 Gbit s^{-1} optical data link test of the device, showing a clear eye opening.

generator used, it was not possible to test the photodetector at higher speeds.

In summary, we have demonstrated a high-performance waveguide-integrated graphene photodetector. The extended interaction length between the graphene and the silicon waveguide optical mode results in a notable photodetection responsivity of 0.108 A W^{-1}, which approaches that of commercial non-avalanche photodetectors[18,25]. We expect that this responsivity could be improved through the following refinements of the design. First, higher graphene absorption for the photodetector may be achieved by extending the graphene length and by coupling the graphene with a transverse magnetic waveguide mode with a stronger evanescent field[16]. Second, the metal-doped junction of the current photodetector gives rise to an internal quantum efficiency as high as 3.8% at zero V_B (ref. 2). We estimate that this efficiency could be improved (by up to 15–30%) by electrically gating the graphene layer to reshape the depth and location of the potential difference[2,20,26]. Third, in future devices, the metal electrode used to dope the graphene junction to couple with the evanescent field of the waveguide may be evaporated to be thinner, which may dope the graphene as efficiently but with lower light absorption into the metal. Such improved designs promise a strong photoresponse for the detector, which is reliable for realistic photonic applications even at zero bias. Moreover, the present device can work with an ultrafast dynamic response at zero-bias operation, allowing low on-chip power consumption. Note that we have fabricated devices on waveguide chips with silicon nitride couplers that show 3 dB fibre-to-waveguide coupling loss. The silicon nitride couplers enable the high-temperature processing steps required in the CMOS process, and high-temperature annealing is also compatible with graphene. In addition, planarization of the photonic integrated circuit enables reliable transfer of wafer-scale graphene with a low probability of rupture, or potentially even growth directly on the entire chip. Therefore, the CMOS-processing compatibility of waveguide-integrated graphene photodetectors appears possible in the near term through (1) the use of chemical vapour deposition grown graphene, either transferred or selectively grown on the waveguide chip[27], and (2) deposition of CMOS-compatible metal to replace gold in the titanium/gold contacts. This waveguide-based graphene photodetector, with the combined advantages of a compact footprint, zero-bias operation and ultrafast responsivity over a broad spectral range, opens the door to high-performance, CMOS-compatible graphene optoelectronic devices in photonic integrated circuits.

Methods

Fabrication of the waveguide-integrated graphene photodetector. The silicon waveguides were fabricated on an SOI wafer with a 220-nm-thick silicon membrane over a 3-μm-thick SiO_2 film using the standard shallow trench isolation (STI) module in CMOS processing. A waveguide width of 520 nm was chosen to ensure a single TE mode with low transmission loss. To prevent the graphene from rupturing at the edges of the waveguide, the chip was planarized by backfilling with a thick SiO_2 layer, followed by chemical mechanical polishing to reach the top silicon layer. An ~10-nm-thick SiO_2 layer was subsequently deposited on the chip to ensure electrical isolation of the graphene layer. A mechanically exfoliated graphene bilayer was deposited onto the waveguide using a precision transfer technique[28]. Patterns for the metal electrodes were defined in a poly(methyl methacrylate) (PMMA) resist using electron-beam lithography, which provided an alignment accuracy of ~10 nm. The two electrodes were placed ~100 nm and 3.5 μm from the edges of the silicon waveguide. Titanium/gold metal layers (1 nm/40 nm thickness) were deposited using electron-beam evaporation to form electrodes after liftoff of the PMMA layer.

Simulation of the guided mode. Simulation of the guided mode was carried out using a finite element method (COMSOL). The structure of the device used in the simulation is shown in Fig. 3a. The thicknesses of the graphene bilayer and gold contacts were taken to be 1.4 nm and 40 nm, respectively. The refractive indices of SiO_2, silicon, gold and graphene were 1.48, 3.4, 0.55 + 11.5i (ref. 29) and 2.38 + 1.68i (ref. 30) for light in the telecommunications wavelength range 1,550 nm, respectively.

Photocurrent measurements. All measurements were performed under ambient conditions. The scanning photocurrent image was measured on a vertical confocal microscope set-up using 1,550 nm laser radiation focused at normal incidence to a spot size of 900 nm. Photocurrent images were collected by scanning an x–y piezo-actuated stage in 100 nm steps. The graphene absorption and photoresponsivity of the device in the waveguide-integrated configuration were measured on an edge-coupling set-up using lensed fibres. A fibre-based polarization controller was used to match the input polarization with the TE guided mode. In both measurements, the incident laser was modulated internally at a frequency of 1 kHz, and the short-circuit photocurrent signal was detected with a current preamplifier and a lock-in amplifier. Here, the excitation laser (HP 8168F) had a tuning range of 1,450–1,590 nm. For measurements of the detector responsivity under pulsed excitation, we used an OPO operating at a wavelength of 2,000 nm and providing 250 fs pulses at a repetition rate of 78 MHz.

Dynamic response of the device. The response rate of the graphene photodetector was characterized using a commercial LCA (Agilent 8703) with an internally modulated laser source and a network analyser. The output of the LCA (at a wavelength of 1,550 nm) was coupled into the photodetector. The photocurrent signal was extracted through a G–S microwave probe with frequency capability up to 40 GHz (Cascade Microtech) and fed back to the input port of the network analyser. The frequency response (scattering parameter S_{21}) was recorded as the optical modulation frequency was swept between 0.13 GHz and 20 GHz. For eye-diagram measurements at a data rate of 12 Gbit s^{-1}, a pulse pattern generator (Anritsu MP1763B) with an internal pseudo-random bit sequence (with a length of 2^{11}– 1) was used to drive a JDS Uniphase Mach–Zehnder modulator to modulate a 1,550 nm c.w. laser. The optical signal was amplified with an erbium-doped fibre amplifier and coupled into the photodetector. The electrical output of the detector passed through a radiofrequency power amplifier (ZVA–183w+) with a gain of 30 dB and bandwidth of 18 GHz, and the eye diagram was recorded using an Agilent DSO81004A wide-band oscilloscope.

References

1. Bonaccorso, F., Sun, Z., Hasan, T. & Ferrari, A. C. Graphene photonics and optoelectronics. *Nature Photon.* **4,** 611–622 (2010).
2. Xia, F., Mueller, T., Lin, Y.-M., Valdes-Garcia, A. & Avouris, P. Ultrafast graphene photodetector. *Nature Nanotech.* **4,** 839–843 (2009).
3. Mueller, T., Xia, F. & Avouris, P. Graphene photodetectors for high-speed optical communications. *Nature Photon.* **4,** 297–301 (2010).
4. Nair, R. R. et al. Fine structure constant defines visual transparency of graphene. *Science* **320,** 1308 (2008).
5. Kotov, V., Uchoa, B., Pereira, V., Guinea, F. & Castro Neto, A. Electron–electron interactions in graphene: current status and perspectives. *Rev. Mod. Phys.* **84,** 1067–1125 (2012).
6. Song, J. C. W., Rudner, M. S., Marcus, C. M. & Levitov, L. S. Hot carrier transport and photocurrent response in graphene. *Nano Lett.* **11,** 4688–4692 (2011).
7. Freitag, M., Low, T., Xia, F. & Avouris, P. Photoconductivity of biased graphene. *Nature Photon.* **7,** 53–59 (2012).
8. Tielrooij, K. J. et al. Photoexcitation cascade and multiple hot-carrier generation in graphene. *Nature Phys.* **9,** 248–252 (2013).
9. Gan, X. et al. Strong enhancement of light–matter interaction in graphene coupled to a photonic crystal nanocavity. *Nano Lett.* **12,** 5626–5631 (2012).
10. Furchi, M. et al. Microcavity-integrated graphene photodetector. *Nano Lett.* **12,** 2773–2777 (2012).
11. Echtermeyer, T. J. et al. Strong plasmonic enhancement of photovoltage in graphene. *Nature Commun.* **2,** 455–458 (2011).
12. Liu, Y. et al. Plasmon resonance enhanced multicolour photodetection by graphene. *Nature Commun.* **2,** 579 (2011).
13. Konstantatos, G. et al. Hybrid graphene quantum dot phototransistors with ultrahigh gain. *Nature Nanotech.* **7,** 363–368 (2012).
14. Urich, A., Unterrainer, K. & Mueller, T. Intrinsic response time of graphene photodetectors. *Nano Lett.* **11,** 2804–2808 (2011).
15. Assefa, S., Xia, F. & Vlasov, Y. A. Reinventing germanium avalanche photodetector for nanophotonic on-chip optical interconnects. *Nature* **464,** 80–84 (2010).
16. Liu, M. et al. A graphene-based broadband optical modulator. *Nature* **474,** 64–67 (2011).
17. Kim, K., Choi, J-Y., Kim, T., Cho, S-H. & Chung, H-J. A role for graphene in silicon-based semiconductor devices. *Nature* **479,** 338–344 (2011).
18. Michel, J., Liu, J. & Kimerling, L. C. High-performance Ge-on-Si photodetectors. *Nature Photon.* **4,** 527–534 (2010).
19. Li, G. et al. Improving CMOS-compatible germanium photodetectors. *Opt. Express* **20,** 26345–26350 (2012).
20. Mueller, T., Xia, F., Freitag, M., Tsang, J. & Avouris, P. Role of contacts in graphene transistors: a scanning photocurrent study. *Phys. Rev. B* **79,** 245430 (2009).
21. Xia, F. et al. Photocurrent imaging and efficient photon detection in a graphene transistor. *Nano Lett.* **9,** 1039–1044 (2009).
22. Mak, K. F., Lui, C. H., Shan, J. & Heinz, T. F. Observation of an electric-field-induced band gap in bilayer graphene by infrared spectroscopy. *Phys. Rev. Lett.* **102,** 256405 (2009).
23. Gan, X. et al. High-contrast electrooptic modulation of a photonic crystal nanocavity by electrical gating of graphene. *Nano Lett.* **13,** 691–696 (2013).
24. Xing, G. et al. The physics of ultrafast saturable absorption in graphene. *Opt. Express* **18,** 4564–4573 (2010).
25. Wang, J. & Lee, S. Ge-photodetectors for Si-based optoelectronic integration. *Sensors* **11,** 696–718 (2011).
26. Park, J., Ahn, Y. H. & Ruiz-Vargas, C. Imaging of photocurrent generation and collection in single-layer graphene. *Nano Lett.* **9,** 1742–1746 (2009).
27. Liu, W. et al. Large scale pattern graphene electrode for high performance in transparent organic single crystal field-effect transistors. *ACS Nano* **4,** 3927–3932 (2010).
28. Dean, C. R. et al. Boron nitride substrates for high-quality graphene electronics. *Nature Nanotech.* **5,** 722–726 (2010).
29. Johnson, P. B. & Christy, R. W. Optical constants of the noble metals. *Phys. Rev. B* **6,** 4370–4379 (1972).
30. Kravets, V. G. et al. Spectroscopic ellipsometry of graphene and an exciton-shifted van Hove peak in absorption. *Phys. Rev. B* **81,** 155413 (2010).

Author contributions

X.G., R.S., S.A. and D.E. conceived and designed the experiments. R.S., Y.G. and X.G. fabricated the devices. S.A., X.G. and D.E. designed and provided waveguide chips; J.H. provided graphene samples. X.G. and R.S. performed the experiments. I.M. and K.S. analysed the high-speed measurements. X.G., D.E. and T.H. prepared the manuscript. All authors commented on the manuscript.

Additional information

Reprints and permissions information is available online at www.nature.com/reprints. Correspondence and requests for materials should be addressed to D.E.

Competing financial interests

Solomon Assefa is at IBM T. J. Watson Research Center, Yorktown Heights, New York 10598, USA.